Supporting information for:

Tunable thermodynamic activity of $La_xSr_{1-x}Mn_yAl_{1-y}O_{3-\delta}$ ($0 \le x \le 1$, $0 \le y \le 1$) perovskites for solar thermochemical fuel synthesis

M. Ezbiri[a,b], M. Takacs[a], D. Theiler[a], R. Michalsky[a,*], A. Steinfeld[a]

[a] Department of Mechanical and Process Engineering, ETH Zürich, 8092 Zürich, Switzerland

[b] Solar Technology Laboratory, Paul Scherrer Institute, 5232 Villigen-PSI, Switzerland

* Email: michalskyr@ethz.ch

Overview Supporting Information

1. Computational details

a. Structure optimizations

Both, ASE and GPAW are open-source codes available from the Department of Physics at the Technical University of Denmark and are available at https://wiki.fysik.dtu.dk/ase/ and https://wiki.fysik.dtu.dk/gpaw/.

Table S1. Calculated lattice constants (a) and magnetic moments of Mn (M) of cubic (space group 221) $La_{0.25}Sr_{0.75}Mn_{0.75}Al_{0.25}O_{3-\delta}$ (LSMA1331), $La_{0.75}Sr_{0.25}Mn_{0.25}Al_{0.75}O_{3-\delta}$ (LSMA3113) and $La_{0.75}Sr_{0.25}Mn_{0.75}Al_{0.25}O_{3-\delta}$ (LSMA3131) perovskites.

Perovskites	a (Å)	M (μ_B)
LSMA1331	3.910	2.875/2.978/2.875
LSMA3113	3.800	2.789
LSMA3131	3.947	3.492/3.491/3.592

We note that the lattice constants computed by DFT compare well, within the uncertainty of DFT calculations, with the experimental values of cubic perovskites with similar composition.[1, 2] For example, the DFT-computed 3.910 Å (LSMA1331) is 2.2% larger than the experimental value 3.825 Å ($La_{0.2}Sr_{0.8}MnO_3$),[3] or 2.79% larger than 3.804 Å ($SrMnO_3$),[3] while 3.800 Å (LSMA3113) and 3.947 Å (LSMA3131) are 2.6% smaller and 1.18% larger than 3.901 Å ($La_{0.75}Sr_{0.25}MnO_3$),[4] respectively.

b. Free energy computations

Free energies of the chemical species i (G_i) were calculated via:[1]

$$G_i(T,P) = N_i\mu_i(T,P) = E_i + U_{ZPE,i} - TS_i(T,P) \qquad \text{* MERGEFORMAT (1)}$$

where T and P are the absolute temperature (298.15 K) and pressure (1.013 bar), N_i is the number of atoms, μ_i is the chemical potential, E_i is the total electronic energy determined from DFT-based structure optimization, $U_{ZPE,i}$ is the zero-point vibrational energy, and S_i is the entropy. Gases are assumed to be ideal, while liberated lattice oxygen is treated using the harmonic approximation where all degrees of freedom are treated as frustrated harmonic vibrations and pressure-volume contributions are neglected. Thermodynamic properties were calculated from vibrational frequencies and standard statistical mechanical equations evaluated through ASE. Free energy corrections of the solids are neglected.[5]

Analogously, the enthalpy of forming oxygen vacancies (ΔH_v[O]) at the surface is defined as:

$$\Delta H_v[\mathrm{O}] = \Delta G_v[\mathrm{O}] + T\Delta S_v[\mathrm{O}] \qquad \text{* MERGEFORMAT (2)}$$

where $\Delta S_v[O]$ is the entropy of forming oxygen vacancies.

Throughout this work, free energies and enthalpies are given relative to the chemical potential of stable H_2O and H_2 in the gas phase, that is, E_O^r is given with:[1]

$$E_O^r = E[H_2O] - E[H_2] \qquad \text{* MERGEFORMAT (3)}$$

where $E[H_2O]$ and $E[H_2]$ are the total electronic energy of reference H_2O and H_2 molecules in the gas phase.

c. Scaling relations

Eq. (5) in the paper is based on data for TiO_2 in rutile crystal structure, Ti_2O_3, Cu_2O, ZnO in wurtzite crystal structure, MoO_3, Ag_2O, cubic $Ba_{0.5}Sr_{0.5}Co_{0.5}Fe_{0.5}$, and cubic $La_{0.5}Sr_{0.5}Co_{0.5}Fe_{0.5}$. Data for cubic ZrO_2, cubic $Y_2Zr_6O_{15}$, yttria-stabilized ZrO_2, CeO_2, and $La_{0.67}Sr_{0.33}MnO_3$ was disregarded due to a large deviation of the oxygen nonstoichiometry (δ) between the thermochemical data for the bulk metal oxides and the DFT-data for the oxygen vacancy formation energetics at the metal oxide surface.[6] That is, differences of factor 16-32 for the nonstoichiometry of ZrO_2 ($\delta = 2$ for the ZrO_2/Zr bulk couple vs. $\delta = 0.0625$ for the $Zr_{16}O_{32}/Zr_{16}O_{31}$ surface model couple), $Y_2Zr_6O_{15}$ ($\delta = 2$ for the ZrO_2/Zr bulk couple vs. $\delta = 0.0625$ for the $Y_4Zr_{12}O_{30}/Y_4Zr_{12}O_{29}$ surface model couple), CeO_2 ($\delta = 1$ for the CeO_2/Ce_2O_3 bulk couple vs. $\delta = 0.0625$ for the $Ce_{16}O_{32}/Ce_{16}O_{31}$ surface model couple), and of factor 3, which is relatively high when compared to the other computed perovskite models, for $La_{0.67}Sr_{0.33}MnO_3$ ($\delta = 1$ for the Mn_2O_3/MnO bulk couple vs. $\delta = 0.33$ for the $La_2SrMn_3O_9/La_2SrMn_3O_8$ surface model couple).

Calculations of $\Delta\bar{g}_O^{o*}$ at 1200 K to 2000 K and $-\Delta\bar{g}_O^{o*}$ at 800 K to 1600 K for metal oxides where the underpinning thermochemical data is not available, namely the perovskites evaluated in this work, were based on the scaling of these two bulk quantities with $\Delta\bar{h}_O^{o*}$ at 298 K and 1 bar across 27 solid metal oxide and six metal/metal oxide pairs. Thermodynamic properties obtained through scaling relations are defined per mole of monoatomic oxygen. The data for the derived linear scaling relations ($R^2 > 0.83$) are shown with Table S2, where a and b represent the following factors in Eq. (6):

$$-\Delta\bar{g}_O^{o*} = a \cdot \frac{\text{kJ mol}_O^{-1}}{\text{kJ mol}_O^{-1}} \Delta\bar{h}_O^{o*} + b \text{ kJ mol}_O^{-1} \qquad \text{* MERGEFORMAT (4)}$$

Table S2. DFT-derived linear scaling factors a and b, based on the scaling of $-\Delta\bar{g}_O^{o*}$ with at 298 K and 1 bar across 27 solid metal oxide and six metal/metal oxide pairs.

T (K)	a	b
800	-0.9622	281.04
900	-0.9633	282.80
1000	-0.9647	284.66
1100	-0.9654	286.23
1200	-0.9652	287.54
1300	-0.9625	288.55
1400	-0.9594	289.43
1500	-0.9551	289.96
1600	-0.9514	290.52

Table S3. DFT-derived linear scaling factors a and b, based on the scaling of $\Delta\bar{g}_O^{o*}$ with at 298 K and 1 bar across 27 solid metal oxide and six metal/metal oxide pairs.

T (K)	a	b
1200	0.9652	-164.32
1300	0.9625	-178.53
1400	0.9594	-192.58
1500	0.9551	-206.23
1600	0.9514	-219.89
1700	0.9452	-232.75
1800	0.9337	-242.08
1900	0.9211	-249.61
2000	0.9100	-256.92

The data for the derived linear scaling relations is given with Table S4, S5 and S6, while Table S7, S8 and S9 give the free energies of the oxide oxidation and oxide reduction that were computed with Eq. (6) ($R^2 > 0.92$) for the three studied perovskite compositions.

2. Supporting data

a. Experimental data

The XRD spectra shown with Figure S1 indicate that all perovskites have a rhombohedral perovskite structure.

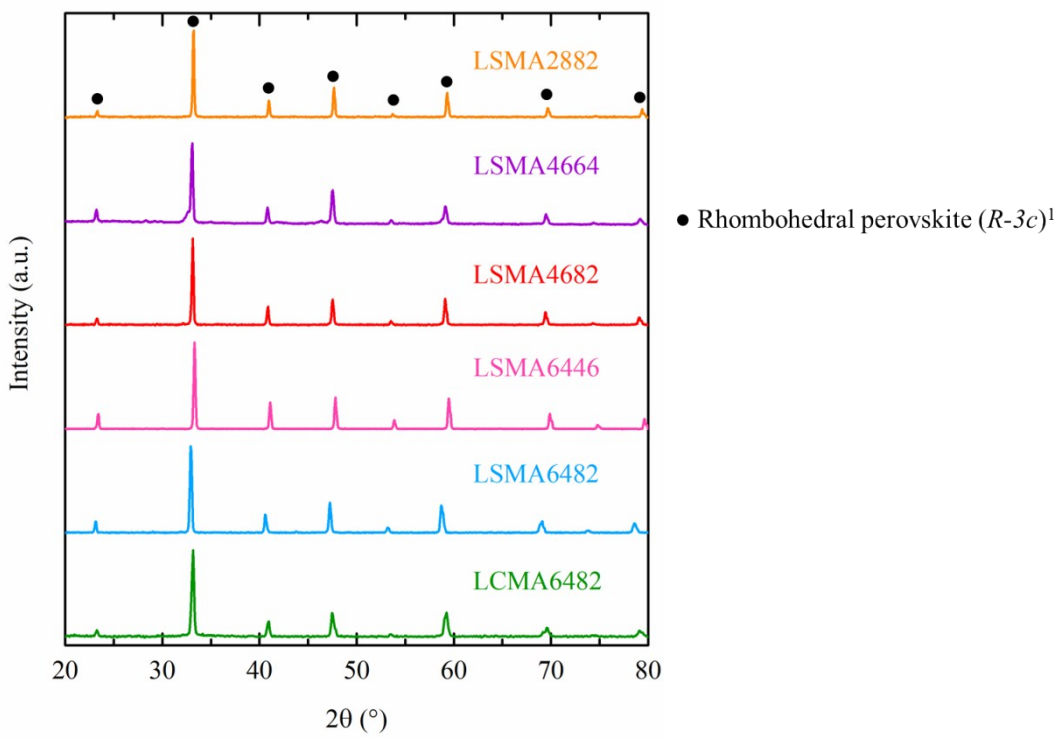

Figure S1: XRD spectra of sintered LSMA2882, LSMA4664, LSMA4682, LSMA6446, LSMA6482 and LCMA6482 (peak labels from Lehnert et al.[7]).

Figures S2 and S3 show the oxygen nonstoichiometry measurements of LSMA6482, LSMA6446, LSMA4664, LSMA4682 and LCMA6482 for T = 1573 K to 1673 K and oxygen partial pressure range pO_2= 0.206 mbar O_2 to 0.900 mbar O_2 (*cf.* Fig. S2) and LSMA2882 for T = 1573 K to 1773 K and pO_2 = 9.48 mbar O_2 to 180 mbar O_2 (*cf.* Fig. S3).

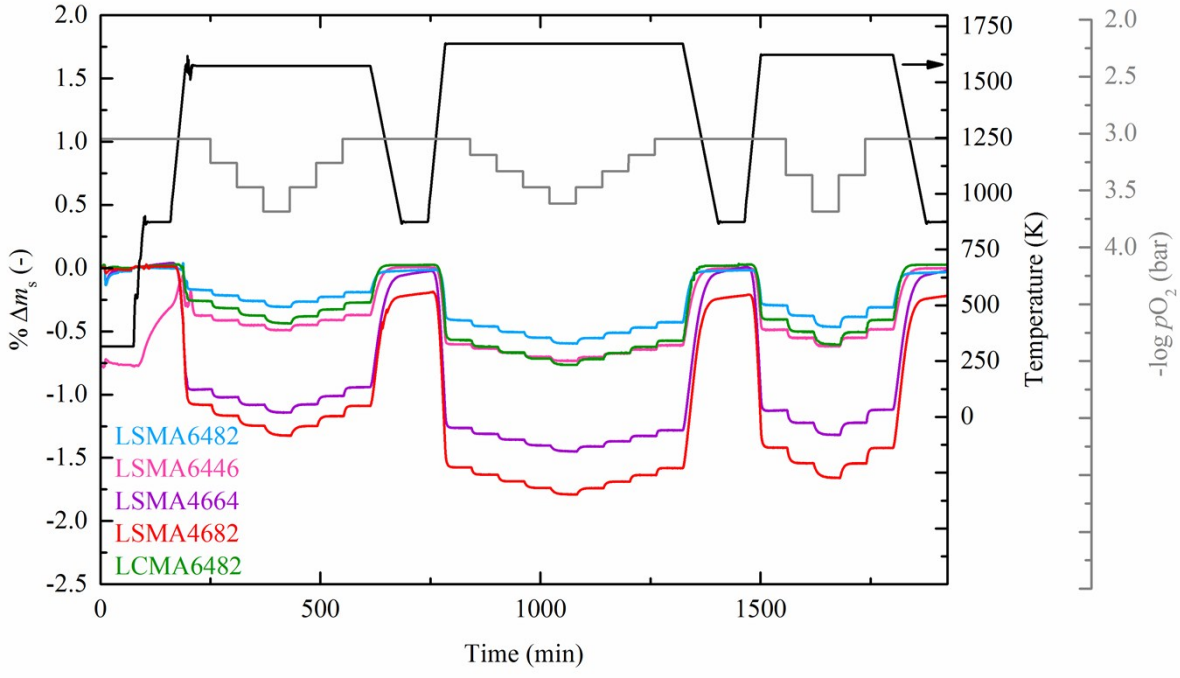

Figure S2: Percent weight change as a function of time for the temperature range T = 1573 K to 1673 K and oxygen partial pressure range pO_2= 0.206 O_2 mbar to 0.900 mbar O_2 of LSMA6446, LSMA6482, LSMA4664, LSMA4682 and LCMA6482.

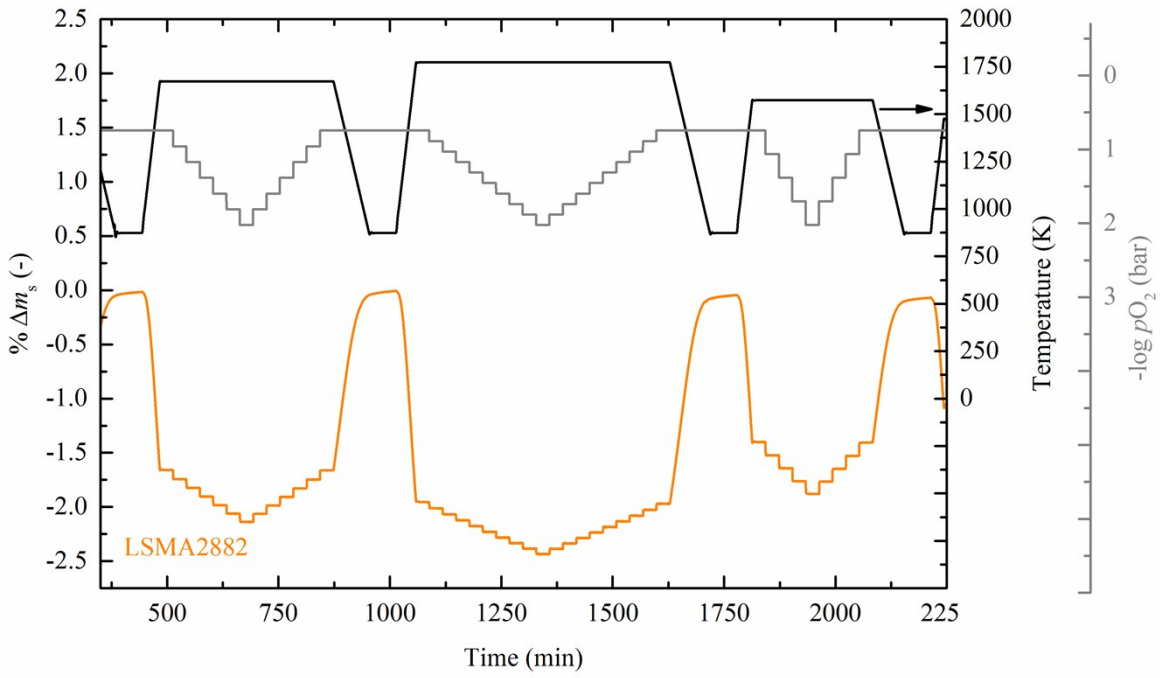

Figure S3: Percent weight change as a function of time for the temperature range T = 1573 K to 1673 K and oxygen partial pressure range pO_2 = 9.48 mbar O_2 to 180 mbar O_2 of LSMA2882.

Experimental determination of the initial oxygen stoichiometry, δ_i:

As outlined by Kuo *et al.*[8], the initial molar oxygen content in perovskites can be determined either at the most or at the least oxidizing reaction condition, as long as stoichiometric compositions are formed only.[8] Following the procedure outlined by the authors, we reduced LSMA2882, the compound with the highest reduction extent, in 2 vol% H_2 in Ar at 1273 K during two hours. XRD showed formation of MnO, $LaMnO_3$, $SrMnO_3$, Sr_2MnO_4 and Al_2O_3. Since $LaMnO_3$ and $SrMnO_3$ are nonstoichiometric compounds, the reducing condition cannot serve as reference state. This is analogous to the discussion of the reference state of Sr-doped $LaMnO_3$ by Kuo *et al.*[8]. However, previously we determined the initial oxygen nonstoichiometry successfully for simpler binary perovskites.[9]

Analysis of the sensitivity of the thermochemical calculations to the assumption δ_i = 0:

The defect model requires necessarily knowledge of the actual perovskite stoichiometry. The initial oxygen stoichiometry δ_i of the quaternary perovskites is unknown in this work. Thus, for the modeling we assumed δ_i = 0. To assess the sensitivity of the thermodynamic calculations on the actual initial oxygen nonstoichiometry, we assumed alternatively δ_i = 0.055 and recalculated the derived thermodynamic quantities. The value δ_i = 0.055 is the arithmetic average of 0.06 and 0.05, which are the actual initial oxygen nonstoichiometries measured for $BaMnO_{2.94}$ and $SrCoO_{2.95}$, respectively.[9] From the investigated binary perovskites,[9] we considered these two compositions as they contain elements that are also contained in the quaternary LSMA compositions investigated here. We find that the computed thermodynamic quantities are relatively insensitive to this change in the value of the initial oxygen nonstoichiometry. For example, recomputing the partial molar Gibbs free energy, shows that oxidation and reduction become thermodynamically favorable at 3 to 8 K lower equilibrium temperatures at δ_i = 0.055, compared to δ_i = 0 (*cf.* Fig. 5). This translates into a negligible relative uncertainty of the computed partial molar Gibbs free energy of 0.2 to 0.5%.

b. Defect modeling

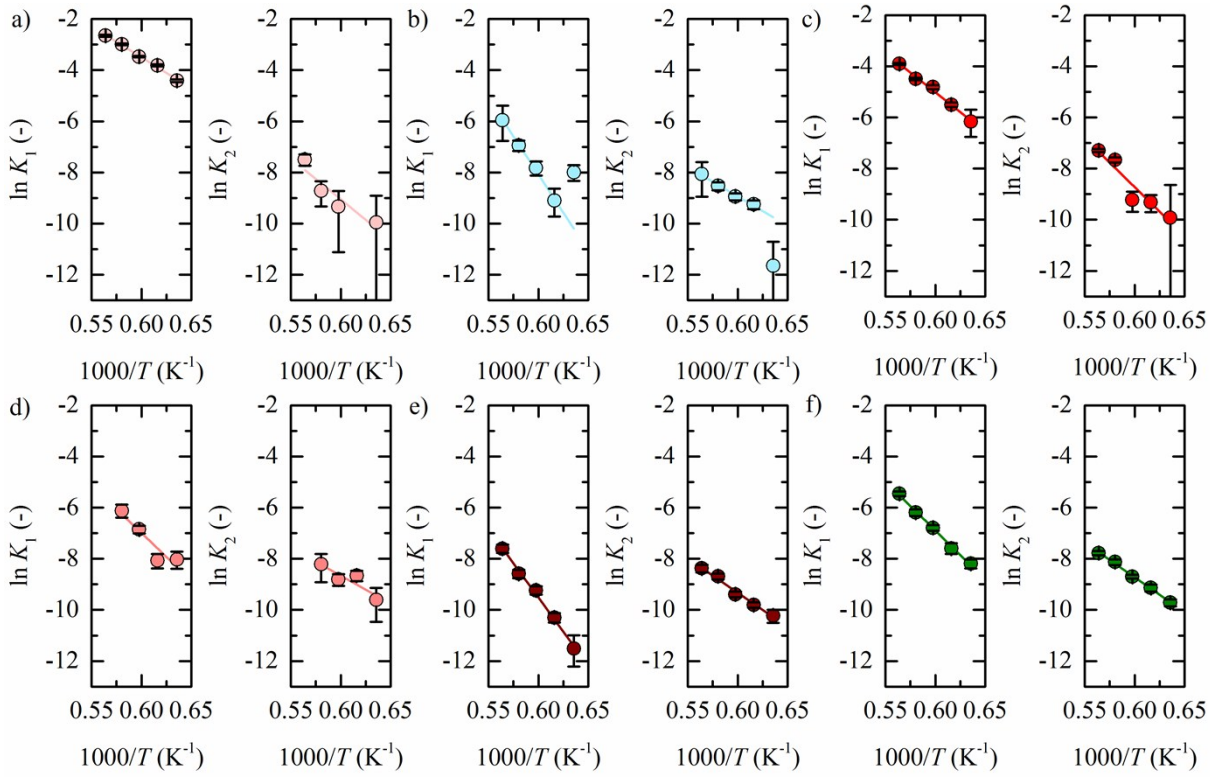

Figure S4: Equilibrium constants $\ln K_1$ (left) and $\ln K_2$ (right) as a function of the inverse temperature for a) LSMA2882, b) LSMA6482, c) LSMA4682, d) LSMA4664, e) LSMA6446 and f) LCMA6482. Lines indicate linear dependence of K_1 and K_2 on 1000/T. Error bars correspond to $\pm 2\sigma$ (two times standard deviation) of $\ln K_1$ and $\ln K_2$.

Using the computed equilibrium constants, as described by Takacs *et al.*,[10] allows the calculation of δ values using arbitrary pO_2 resulting in the solid black lines and the dashed colored lines shown with Figures 2 and S5. The solid black lines were calculated using the individual data points while the dashed colored lines were determined using the inverse linear temperature dependence of $\ln K_1$ and $\ln K_2$.

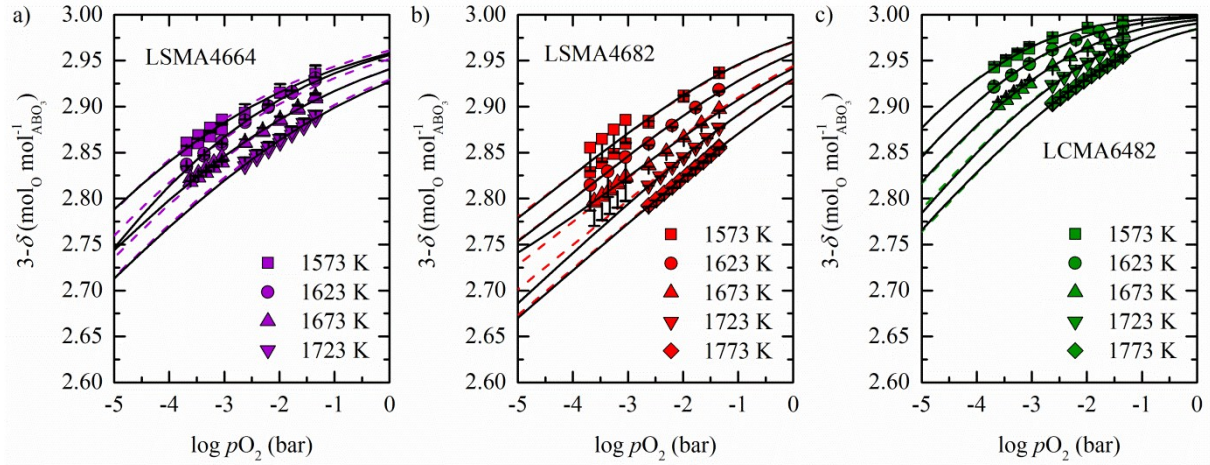

Figure S5: Measured oxygen exchange capacity (symbols) of a) LSMA4664, b) LSMA4682 and c) LCMA6482 as a function of pO_2 for T = 1573 K to 1773 K. Colored dashed and black solid lines are calculated values based on the defect model used to describe the experimental results. Black solid lines are calculated based on individual defect equilibrium constants, while colored dashed lines are calculated by using the inverse temperature dependence of $\ln K_1$ and $\ln K_2$. Error bars correspond to mass deviations from zero at the stabilization steps of 873 K.

Plots showing $-\ln(pO_2/p^o)$ as a function of $1/T$ are displayed in Figure S6, allowing for the extraction of enthalpy and entropy as slope and intercept, respectively.

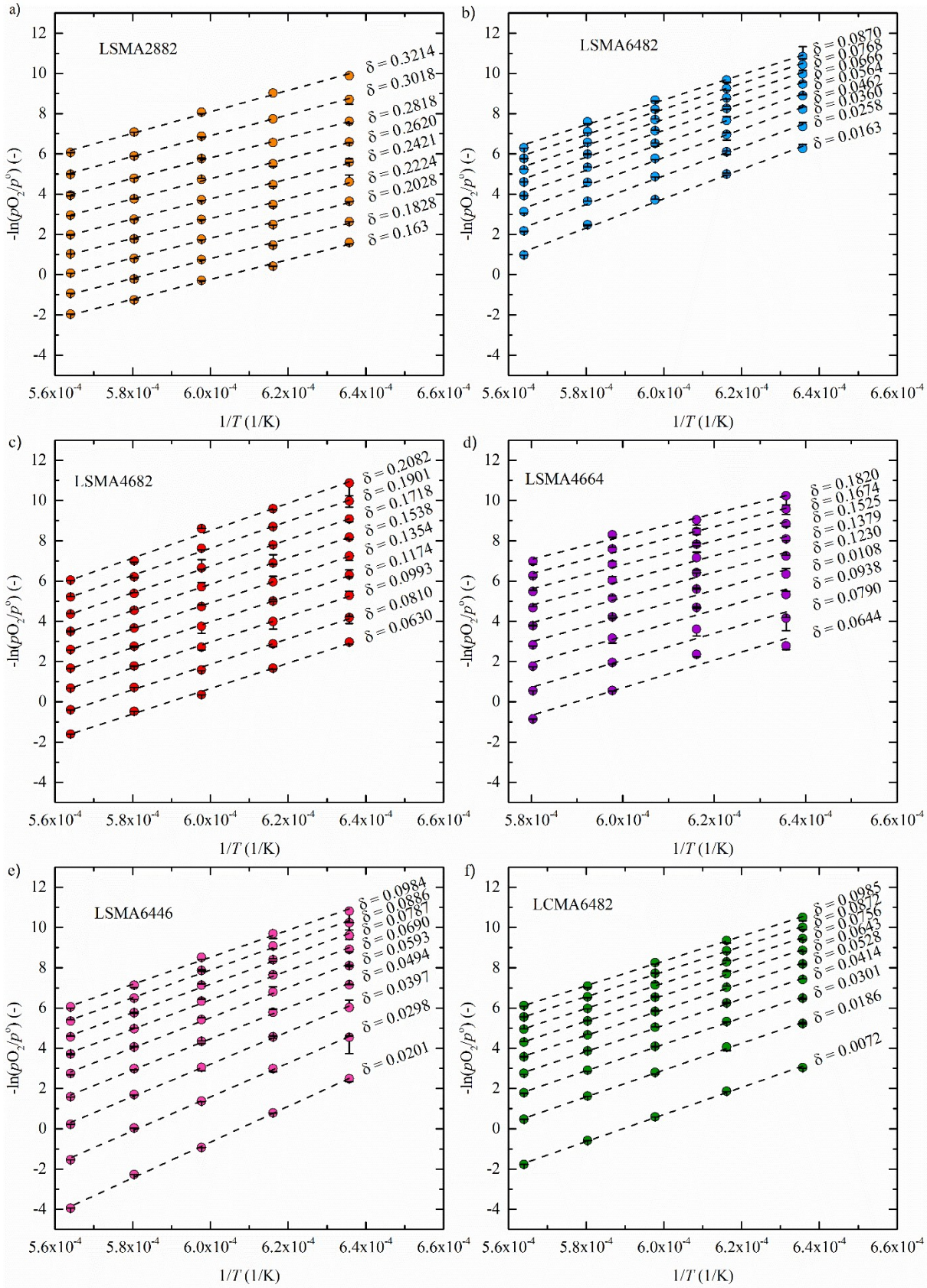

Figure S6: -ln(pO_2/p^o) as a function of 1/T of a) LSMA2882 for δ = 0.1630 – 0.3214, b) LSMA6482 for δ = 0.0163 – 0.0870, c) LSMA4682 for δ = 0.0630 – 0.2082, d) LSMA4664 for δ = 0.0644 – 0.1820, e) LSMA6446 for δ = 0.0201 – 0.0984 and f) LCMA6482 for δ = 0.0072 – 0.0985 for the temperature range T = 1573 K to 1773 K and oxygen nonstoichiometry range δ = 0.0198 to 0.0984. Error bars correspond to deviations between measured and fitted pO_2 illustrated in Fig. 2, while the symbols correspond to the black lines shown in Fig. 2.

c. Thermodynamics

Figures S7 and S8 show $\Delta\bar{h}_O^\circ$ (*cf.* Figs. S7a and S7b), $\Delta\bar{s}_O^\circ$ (*cf.* Figs. S7c and S7d) and $\Delta\bar{g}_O^\circ$ (*cf.* Fig. S8) of LSMA4664, LSMA4682, LSMA6464[10], LCMA6464[10] and LCMA6482. In the case of the LSMA compounds we can see that changing the B-cation ratio (LSMA4664 and LSMA4682) does not significantly affect $\Delta\bar{g}_O^\circ$, while varying the A-cation ratio (LSMA4664 and LSMA6464[10]) does (*cf.* Fig. S8a), confirming the thermodynamic results of the main document. Furthermore, the same trend is observed when Sr is replaced by Ca. $\Delta\bar{g}_O^\circ$ of LCMA6464[10] and LCMA6482 are very similar (*cf.* Fig. S8b).

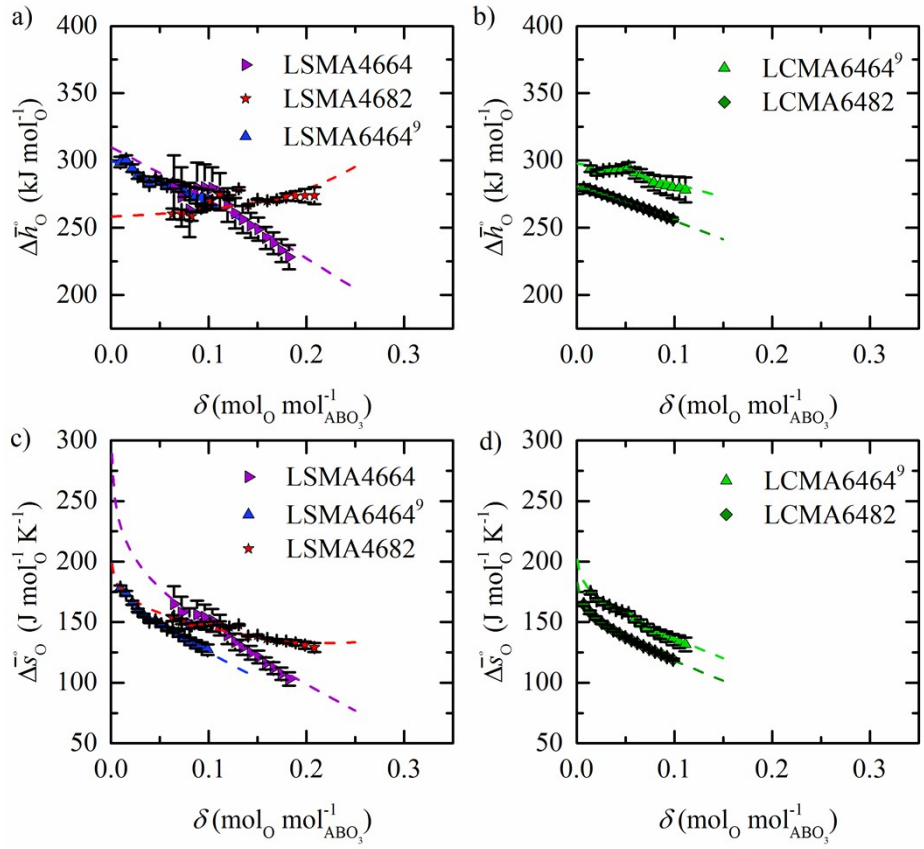

Figure S7: Standard partial molar enthalpy $\Delta\bar{h}_O^\circ$ and standard partial molar entropy $\Delta\bar{s}_O^\circ$ as a function of δ for LSMA4664, LSMA4682 and LSMA6464[10] (a) and c), respectively); and for LCMA6464[10] and LCMA6482 (b) and d), respectively). Symbols represent measured values calculated from δ values shown by the black solid lines and the dashed lines are modeled values based on δ values computed from the colored dashed lines of Figures S4a, S4b and S4c. Data for LSMA6464 and LCMA6464 was extracted from the publication by Takacs *et al*.[10]

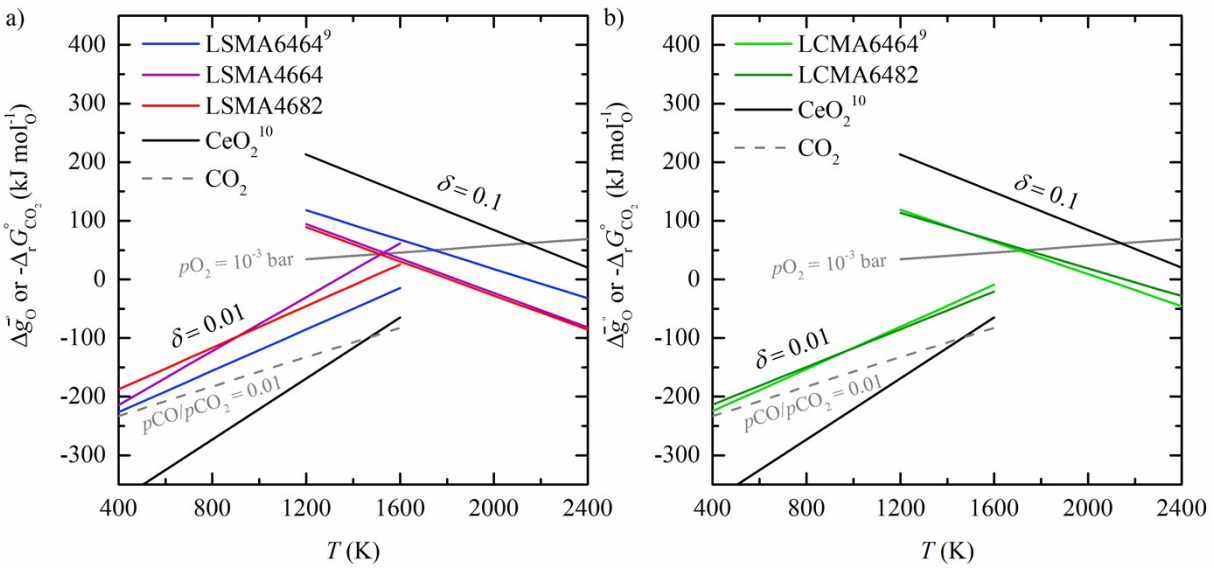

Figure S8: Standard partial molar Gibbs free energy $\Delta\bar{g}^{o}_{O}$ as a function of T for a) LSMA6446, LSMA6464[10], LSMA6482 and CeO_2[11]; and b) LSMA6482, LSMA4682, LSMA2882 and CeO_2[11], for $\delta = 0.10$, relevant for the reduction, and $\delta = 0.01$, relevant for the oxidation. Dashed grey lines represent the Gibbs free energy change of the CO oxidation reaction, $-\Delta_r G^{o}_{CO_2}$ ($CO + 0.5O_2 = CO_2$) in 1% CO in CO_2 ($pCO/pCO_2 = 0.01$). The metal oxide reduction reaction is at equilibrium in $pO_2 = 10^{-3}$ bar at $\delta = 0.10$ at temperatures where $\Delta\bar{g}^{o}_{O}(\Delta\delta = 0.10) = -\frac{1}{2}RT\ln(pO_2 / p^{o})$. Oxidation with CO_2 to $\delta = 0.01$ at $pCO/pCO_2 = 0.01$ is thermodynamically favorable at temperatures where $-\Delta\bar{g}^{o}_{O} = -\Delta_r G^{o}_{CO_2}$.

Thermochemical equilibrium analysis

Thermochemical data[11] was extrapolated for $Ce_2O_3 \geq 1300$ K, $Co_3O_4 \geq 1300$ K, $CuO \geq 1400$ K, $Fe_2O_3 \geq 1800$ K, $Mn_3O_4 \geq 1900$ K, $Mn_2O_3 \geq 1500$ K, $MoO_3 \geq 1500$ K, $Na_2O_2 \geq 1000$ K, $RhO \geq 1200$ K, $Rh_2O_3 \geq 1400$ K, $RuO_2 \geq 1400$ K, $Sb_2O_3 \geq 1800$ K, $SbO_2 \geq 1300$ K, $SnO \geq 1400$ K, $SnO_2 \geq 1600$ K, $Tl_2O \geq 1100$ K, and $Tl_2O_3 \geq 1200$ K using second-order polynomial regressions with R^2 between 0.99932 and 0.99998.

Table S4. Enthalpies of reduction at 298 K ($\Delta\bar{h}^{o*}_{0}$) and Gibbs free energies of the oxide reduction at 298 K ($\Delta\bar{g}^{o*}_{O}$) and oxide oxidation at 298 K ($-\Delta\bar{g}^{o*}_{O}$) of 27 solid metal oxide and six metal/metal oxide pairs at 1 bar, calculated from experiment-derived tabulated thermochemical data.[12]

Product of the oxide oxidation	Reactant of the oxide oxidation	$\Delta\bar{h}^{o*}_{0}$ (kJ mol^{-1}_{O})	$\Delta\bar{g}^{o*}_{O}$ (kJ mol^{-1}_{O})	$-\Delta\bar{g}^{o*}_{O}$ (kJ mol^{-1}_{O})
Ag_2O	Ag	31.1	10.81	246.37
Au_2O_3	Au	-26.92	-25.93	283.11
CeO_2	Ce_2O_3	381.16	342.83	-85.65
Co_3O_4	CoO	196.19	152.31	104.88
Cu_2O	Cu	118.89	108.53	148.655
CuO	Cu_2O	175.81	147.62	109.56
$Fe_{0.947}O$	FeO	302.25	260.9	-3.72
Fe_2O_3	Fe_3O_4	235.98	196.42	60.76
Fe_3O_4	FeO	232.14	194.54	62.65
Mn_3O_4	MnO	101.41	76.88	180.31
Mn_2O_3	Mn_3O_4	156.15	134.95	122.24

MoO_3	MoO_2	95.23	70.54	186.65
Na_2O_2	Na_2O	375.31	347.25	-90.07
NbO_2	NbO	309.62	287.47	-30.28
Nb_2O_5	NbO_2	172.51	165.91	91.28
Rh_2O_3	RhO	152.51	126.51	130.67
RuO_2	Ru	169.04	159.85	97.34
SbO_2	Sb_2O_3	295.05	263.15	-5.97
SnO_2	SnO	435.55	407.27	-150.08
Ti_2O_3	TiO	355.64	333.12	-75.93
Ti_3O_5	Ti_2O_3	376.98	369.87	-112.69
Ti_4O_7	Ti_3O_5	374.47	344.61	-87.42
TiO_2	Ti_4O_7	92.7	81.36	175.82
Tl_2O_3	Tl_2O	355.22	330.63	-73.44
V_2O_3	VO	208.36	179.4	77.78
V_2O_4	V_2O_3	123.43	100.9	156.28
V_2O_5	V_2O_4	265.92	242.73	14.45
$WO_{2.72}$	WO_2	216.17	193.83	63.35
$WO_{2.9}$	$WO_{2.72}$	248.25	225.17	32.02
$WO_{2.96}$	$WO_{2.9}$	198.75	175.64	81.54
WO_3	$WO_{2.96}$	170.71	147.68	109.51
ZnO	Zn	350.46	320.48	-63.29
ZrO_2	Zr	548.73	519.86	-262.68

Table S5. Gibbs free energies of the oxide oxidation between 800 K and 1600 K ($-\Delta\bar{g}_O^{o*}$) of 27 solid metal oxide and six metal/metal oxide pairs at 1 bar, calculated from experiment-derived tabulated thermochemical data.[12]

		$-\Delta\bar{g}_O^{o*}$ (kJ mol_O^{-1})								
Product of the oxide oxidation	**Reactant of the oxide oxidation**	**800 K**	**900 K**	**1000 K**	**1100 K**	**1200 K**	**1300 K**	**1400 K**	**1500 K**	**1600 K**
Ag_2O	Ag	245.46	248.62	252.67	257.51	263.11	270.64	279.49	288.97	299.05
Au_2O_3	Au	288.78	291.54	294.74	298.33	302.31	306.64	311.70	317.30	323.19
CeO_2	Ce_2O_3	-62.90	-57.93	-52.81	-47.57	-42.19	-33.67	-25.22	-15.74	-5.18
Co_3O_4	CoO	143.81	152.16	160.40	168.42	176.17	181.25	186.16	189.99	192.69
CuO	Cu_2O	156.86	157.86	158.71	159.44	160.04	160.54	158.63	156.93	157.99
Cu_2O	Cu	109.86	109.63	109.41	109.22	109.04	108.89	108.78	108.62	108.47
$Fe_{0.947}O$	FeO	19.17	21.94	24.33	26.64	28.95	31.34	33.84	36.45	39.16
Fe_2O_3	Fe_3O_4	85.58	91.82	97.85	103.63	109.41	115.11	120.71	126.18	131.57
Fe_3O_4	FeO	82.13	85.84	89.47	93.01	96.44	99.76	102.95	105.34	107.08
Mn_3O_4	MnO	176.54	175.60	174.62	173.60	172.55	171.45	170.31	161.24	155.09
Mn_2O_3	Mn_3O_4	112.49	110.34	108.15	104.77	97.84	90.76	83.56	76.45	67.44
MoO_3	MoO_2	182.10	180.20	177.41	174.03	169.80	165.14	159.86	156.71	152.62
Na_2O_2	Na_2O	-88.47	-88.56	-88.79	-89.20	-90.05	-91.01	-92.01	-93.05	-94.12
NbO_2	NbO	-37.78	-39.20	-40.46	-41.44	-41.61	-41.62	-41.56	-41.44	-41.28
Nb_2O_5	NbO_2	108.09	111.63	115.23	118.86	124.32	129.84	133.54	138.28	143.13
Rh_2O_3	RhO	128.47	127.74	126.95	126.13	125.26	124.36	122.56	120.86	118.90
RuO_2	Ru	110.75	114.46	122.91	133.25	143.64	151.67	159.83	167.21	173.72
SbO_2	Sb_2O_3	2.17	3.08	3.89	4.65	5.36	6.03	7.81	9.40	8.60
SnO_2	SnO	-150.97	-151.99	-153.12	-154.33	-155.57	-156.58	-157.15	-157.68	-158.14
Ti_2O_3	TiO	-96.05	-99.61	-102.66	-105.28	-107.58	-109.64	-111.52	-113.30	-115.03
Ti_3O_5	Ti_2O_3	-103.40	-99.46	-95.91	-92.63	-89.50	-86.40	-83.23	-79.91	-76.35
Ti_4O_7	Ti_3O_5	-80.02	-78.14	-76.08	-73.86	-71.48	-68.94	-66.25	-63.40	-60.41
TiO_2	Ti_4O_7	180.28	181.76	184.18	186.06	187.48	189.36	191.31	193.32	195.39
Tl_2O_3	Tl_2O	-77.01	-77.83	-78.62	-79.37	-80.08	-80.74	-81.35	-81.91	-82.42

V_2O_3	VO	69.64	67.60	65.53	63.45	61.37	59.29	57.22	55.18	53.17
V_2O_4	V_2O_3	161.63	162.77	159.98	154.16	148.29	142.39	136.48	130.58	124.71
V_2O_5	V_2O_4	7.94	6.43	4.89	3.34	1.76	0.15	-1.47	-3.10	-4.74
$WO_{2.72}$	WO_2	55.37	53.54	51.69	49.81	47.94	46.07	44.21	42.36	40.52
$WO_{2.9}$	$WO_{2.72}$	25.30	23.65	21.99	20.30	18.55	16.80	15.03	13.24	11.44
$WO_{2.96}$	$WO_{2.9}$	77.73	77.17	76.49	73.94	70.36	67.52	65.33	63.65	62.45
WO_3	$WO_{2.96}$	102.62	101.04	99.38	97.64	95.83	93.92	92.75	92.62	88.96
ZnO	Zn	-56.70	-54.66	-52.60	-50.54	-46.39	-34.61	-22.91	-11.30	0.24
ZrO_2	Zr	-259.32	-258.86	-258.42	-257.99	-257.46	-256.88	-256.32	-255.82	-255.47

Table S6. Gibbs free energies of the oxide reduction between 1200 K and 2000 K ($\Delta\bar{g}^{\circ *}_{O}$) of 27 solid metal oxide and six metal/metal oxide pairs at 1 bar, calculated from experiment-derived tabulated thermochemical data.[12]

		$\Delta\bar{g}^{\circ *}$ (kJ mol_O^{-1})								
Product of the oxide oxidation	**Reactant of the oxide oxidation**	**1200 K**	**1300 K**	**1400 K**	**1500 K**	**1600 K**	**1700 K**	**1800 K**	**1900 K**	**2000 K**
Ag_2O	Ag	-84.90	-101.05	-118.47	-136.50	-155.09	-174.22	-193.85	-213.96	-234.52
Au_2O_3	Au	-124.09	-137.04	-150.68	-164.83	-179.23	-193.88	-208.77	-223.87	-239.17
CeO_2	Ce_2O_3	220.40	203.27	186.24	168.21	149.14	128.98	107.67	85.18	61.48
Co_3O_4	CoO	2.04	-11.66	-25.14	-37.52	-48.74	-58.72	-67.44	-74.83	-80.87
CuO	Cu_2O	18.17	9.05	2.39	-4.46	-14.03	-23.18	-31.52	-39.03	-45.66
Cu_2O	Cu	69.17	60.70	52.24	43.85	35.49	31.64	32.23	32.90	33.62
$Fe_{0.947}O$	FeO	149.26	138.25	127.18	116.03	104.80	91.30	75.51	61.84	53.28
Fe_2O_3	Fe_3O_4	68.80	54.49	40.31	26.29	12.39	-1.40	4.15	-1.70	-15.24
Fe_3O_4	FeO	81.77	69.84	58.06	47.13	36.88	26.71	16.62	12.32	6.41
Mn_3O_4	MnO	5.66	-1.85	-9.29	-8.77	-11.13	-11.24	-8.97	-15.55	-16.13
Mn_2O_3	Mn_3O_4	80.37	78.84	77.46	76.03	76.52	78.10	80.80	84.63	89.62
MoO_3	MoO_2	8.41	4.46	1.16	-4.23	-8.66	-11.88	-13.85	-14.54	-13.90
Na_2O_2	Na_2O	268.26	260.60	253.03	245.52	238.08	230.68	223.32	215.99	208.68
NbO_2	NbO	219.82	211.22	202.58	193.92	185.24	176.54	168.71	166.05	163.69

Nb_2O_5	NbO_2	53.90	39.75	27.48	14.19	0.83	-12.60	-26.08	-39.62	-53.21
Rh_2O_3	RhO	52.95	45.24	38.45	31.62	25.06	18.79	12.82	7.15	1.80
RuO_2	Ru	34.57	17.93	1.19	-14.74	-29.77	-43.82	-68.16	-87.72	-107.76
SbO_2	Sb_2O_3	172.85	163.57	153.21	143.07	135.36	126.68	118.21	109.95	101.91
SnO_2	SnO	333.78	326.18	318.17	310.15	302.10	294.02	285.87	277.64	269.33
Ti_2O_3	TiO	285.79	279.23	272.54	265.77	258.99	252.25	245.59	239.06	232.69
Ti_3O_5	Ti_2O_3	267.71	255.99	244.25	232.38	220.31	207.96	195.26	182.15	186.05
Ti_4O_7	Ti_3O_5	249.70	238.54	227.27	215.87	204.37	192.75	181.02	169.18	151.40
TiO_2	Ti_4O_7	-9.27	-19.76	-30.29	-40.85	-51.43	-62.03	-72.64	-83.25	-93.86
Tl_2O_3	Tl_2O	258.29	250.33	242.36	234.38	226.38	218.37	210.36	202.33	194.29
V_2O_3	VO	116.85	110.31	103.80	97.30	90.79	84.28	77.76	76.33	76.16
V_2O_4	V_2O_3	29.92	27.21	24.54	21.89	19.25	16.61	13.94	6.13	-3.01
V_2O_5	V_2O_4	176.46	169.44	162.49	155.57	148.70	141.84	134.98	128.12	121.23
$WO_{2.72}$	WO_2	130.27	123.52	116.81	110.12	103.44	96.78	90.13	83.49	76.86
$WO_{2.9}$	$WO_{2.72}$	159.66	152.80	145.99	139.23	132.52	125.86	119.20	112.61	106.04
$WO_{2.96}$	$WO_{2.9}$	107.85	102.08	95.69	88.82	81.51	73.88	124.37	224.60	327.36
WO_3	$WO_{2.96}$	82.38	75.68	68.26	59.85	55.00	50.61	46.33	42.15	38.07
ZnO	Zn	224.61	204.21	183.93	163.77	143.72	123.78	103.95	84.23	64.60
ZrO_2	Zr	435.67	426.48	417.34	408.29	399.43	390.60	381.78	372.98	364.18

d. Electronic structure calculations

Table S7. DFT-calculated free energies of forming oxygen vacancies at 298 K (ΔG_v[O]) and enthalpies of the oxide reduction at 298 K ($\Delta\bar{h}_O^{o*}$) for LSMA1331(010), LSMA3131(010) and LSMA3113(010) perovskite facets. All data is at 1 bar.

Perovskites	**ΔG_v[O] (eV)**	$\Delta\bar{h}_O^{o*}$ **(kJ mol$_O^{-1}$)**
LSMA1331	0.65	163.13
LSMA3131	2.07	321.81
LSMA3113	2.12	327.26

Table S8. DFT-calculated standard partial molar Gibbs free energies of the oxide reduction between 1200 K and 2000 K ($\Delta\bar{g}_O^{o*}$) for LSMA1331(010), LSMA3131(010) and LSMA3113(010) perovskite facets. All data is at 1 bar.

	***T* (K)**	**LSMA1331**	**LSMA3131**	**LSMA3113**
$\Delta\bar{g}_O^{o*}$ **(kJ mol$_O^{-1}$)**	**1200**	-6.87	146.28	151.54
	1300	-21.52	131.21	136.45
	1400	-36.07	116.16	121.39
	1500	-50.42	101.14	106.34
	1600	-64.69	86.28	91.46
	1700	-78.56	71.42	76.57
	1800	-89.76	58.40	63.49
	1900	-99.35	46.81	51.83
	2000	-108.47	35.92	40.87

Table S9. DFT-calculated standard partial molar Gibbs free energies of the oxide oxidation between 800 K and 1600 K ($-\Delta\bar{g}_O^{o*}$) for LSMA1331(010), LSMA3131(010) and LSMA3113(010) perovskite facets. All data is at 1 bar.

	***T* (K)**	**LSMA1331**	**LSMA3131**	**LSMA3113**
$-\Delta\bar{g}_O^{o*}$ **(kJ mol$_O^{-1}$)**	**800**	124.08	-28.60	-33.84
	900	125.66	-27.20	-32.44
	1000	127.29	-25.79	-31.04
	1100	128.73	-24.46	-29.72
	1200	130.08	-23.07	-28.33
	1300	131.53	-21.20	-26.44
	1400	132.93	-19.31	-24.53
	1500	134.14	-17.41	-22.62
	1600	135.31	-15.66	-20.84

3. References

1. A. J. Medford, A. Vojvodic, F. Studt, F. Abild-Pedersen and J. K. Nørskov, *J. Catal.*, 2012, **290**, 108-117.
2. R. Michalsky, Y. J. Zhang, A. J. Medford and A. A. Peterson, *J. Phys. Chem. C*, 2014, **118**, 13026-13034.
3. O. Chmaissem, B. Dabrowski, S. Kolesnik, J. Mais, J. D. Jorgensen and S. Short, *Phys. Rev. B*, 2003, **67**.
4. M. J. Sayagues, J. M. Cordoba and F. J. Gotor, *J. Solid State Chem.*, 2012, **188**, 11-16.
5. Z. H. Zeng, F. Calle-Vallejo, M. B. Mogensen and J. Rossmeisl, *PCCP*, 2013, **15**, 7526-7533.
6. R. Michalsky, V. Botu, C. M. Hargus, A. A. Peterson and A. Steinfeld, *Adv. Energy Mater.*, 2014, **4**, 1401082.
7. H. Lehnert, H. Boysen, J. Schneider, F. Frey, D. Hohlwein, P. Radaelli and H. Ehrenberg, *Z. Kristallogr.*, 2000, **215**, 536-541.
8. J. H. Kuo, H. U. Anderson and D. M. Sparlin, *J. Solid State Chem.*, 1989, **83**, 52-60.
9. M. Ezbiri, K. M. Allen, M. E. Gàlvez, R. Michalsky and A. Steinfeld, *Chemsuschem*, 2015, **8**, 1966-1971.
10. M. Takacs, M. Hoes, M. Caduff, T. Cooper, J. R. Scheffe and A. Steinfeld, *Acta Mater.*, 2016, 700-710.
11. M. Takacs, J. R. Scheffe and A. Steinfeld, *PCCP*, 2015, **17**, 7813-7822.
12. I. Barin, *Thermochemical Data of Pure Substances*, 1993.